Highly Conductive, CeramicRich Hybrid Ionogel Electrolytes for RoomTemperature LiMetal Batteries

Original
Highly Conductive, CeramicRich Hybrid Ionogel Electrolytes for RoomTemperature LiMetal Batteries / Zhang, Ying; Bartoli, Mattia; Elia, Giuseppe Antonio; Gerbaldi, Claudio. - In: CHEMELECTROCHEM. - ISSN 2196-0216. - 13:3(2026). [10.1002/celc.202500411]

Publisher:
John Wiley and Sons Inc

Published
DOI:10.1002/celc.202500411

ChemElectroChem

Chemistry Europe
European Chemical Societies Publishing
ChemElectroChem

RESEARCH ARTICLE OPEN ACCESS

Highly Conductive, Ceramic-Rich Hybrid Ionogel Electrolytes for Room-Temperature Li-Metal Batteries

Ying Zhang[1,2] | Mattia Bartoli[3] | Giuseppe Antonio Elia[1,2] | Claudio Gerbaldi[1,2]

[1]GAME Lab - Department of Applied Science and Technology (DISAT), Politecnico di Torino, Torino, Italy | [2]National Reference Centre for Electrochemical Energy Storage (GISEL), INSTM, Firenze, Italy | [3]Center for Sustainable Future Technologies (CSFT@POLITO), Istituto Italiano di Tecnologia, Torino, Italy

Correspondence: Ying Zhang (ying.zhang@polito.it) | Claudio Gerbaldi (claudio.gerbaldi@polito.it)

Received: 23 October 2025 | **Revised:** 11 January 2026 | **Accepted:** 12 January 2026

Keywords: hybrid solid electrolyte | ionic liquid | lithium battery | LLZO | polymer electrolyte

ABSTRACT

Hybrid solid electrolytes present a promising class for applications in lithium-metal batteries; however, their practical implementation remains limited by the difficulty of simultaneously achieving high room-temperature ionic conductivity, mechanical robustness, and stable electrode-electrolyte interfaces. In this study, we report the development of ceramic-rich hybrid ionogels (HIGs) formulated by combining a dimethacrylate polymer with a high content of $Li_{6.25}Al_{0.25}La_3Zr_2O_{12}$ (LLZO) nanoparticles and imidazolium-based ionic liquid electrolytes (ILEs). This approach results in a garnet-rich solid electrolyte matrix intended to balance mechanical integrity and ion-conducting performance. Four groups of self-standing HIG electrolyte membranes are fabricated through an in situ solvent-free thermal polymerization process, where the ILEs feature either single- or binary-anion environments and serve as the reaction media. Comprehensive characterization demonstrates electrolyte membranes with high ionic conductivities (up to 1.93×10^{-3} S cm^{-1} at 20°C). Among the investigated formulations, the LiTFSI-EMIFSI-based HIG exhibits the most favorable electrochemical performance, including a wide electrochemical stability window and stable charge-discharge cycling with $LiFePO_4$ at room temperature, delivering specific discharge capacities approaching 130 mAh g^{-1} up to C/5 and coulombic efficiency close to 100%. This work highlights the potential of hybrid ionogel electrolytes, clarifies the role of anion chemistry in enabling practical solid-state electrolyte designs, and provides a useful strategy for the development of safer and more stable lithium-metal batteries operating at room temperature.

1 | Introduction

In recent years, we have witnessed a rise in the relevance of electrochemical energy storage due to the push for electrification of energy production and mobility. Secondary batteries have become highly relevant among different energy storage devices thanks to their wide range of capabilities that support many modern applications, including electromobility and stationary storage [1]. In the quest for safer, more efficient, and higher-performance Li-based batteries, the development of innovative electrolytes is of predominant importance, and solid-state electrolytes (SSEs) represent an advancement in this area, offering operation improvements over commercial applications of lithium batteries based on flammable organic electrolyte systems that might cause serious safety problems [2–6]. Furthermore, SSEs have the potential to facilitate increased energy densities, which is an important aspect of applications that necessitate high power and a long battery life/range, such as large-scale energy storage systems and electric vehicles [7–9].

Within various SSEs, solid polymer electrolytes (SPEs) offer enhanced safety and electrode compatibility benefits; however, their practical implementation is hindered by a low ionic conductivity at room temperature and a limited electrochemical stability window, restricting their use in advanced energy systems

[10, 11]. In contrast, solid inorganic electrolytes (SIEs), particularly garnet-type lithium lanthanum zirconates such as $Li_{6.25}Al_{0.25}La_3Zr_2O_{12}$ (LLZO), exhibit higher intrinsic lithium-ion conductivity and good electrochemical stability; however, they are generally multicrystalline systems with grain boundaries, pores, and microcracks that impede homogeneous Li^+ transport, leading to ion depletion and polarization and promoting lithium dendrite propagation [12, 13]. In addition, the inherent brittleness of dense ceramic electrolytes poses challenges for interfacial contact and practical cell assembly. To reconcile the complementary advantages and limitations of SPEs and SIEs, research efforts have focused on developing hybrid solid electrolytes, in which polymeric and inorganic components are combined to achieve balanced ionic conductivity, mechanical integrity, and battery performance stability [5, 10, 14–16].

Within hybrid electrolyte systems, ionogels have emerged as a particularly promising subclass of quasi-solid electrolytes. Ionogels are typically formed by confining a room-temperature ionic liquid (RTIL) or an RTIL-based electrolyte solution within a solid host matrix, which may be polymeric, inorganic, or hybrid in nature [17–20]. This architecture can preserve the advantageous physicochemical properties of the ILs, such as high ionic conductivity, negligible vapor pressure, and wide electrochemical stability windows, while the solid matrix provides mechanical properties and processability into self-standing membranes.

The incorporation of ionic liquids has therefore been widely regarded as an effective strategy for improving the electrochemical performance in solid-state battery systems [21–23]. For instance, Zhai et al. demonstrated that combining ILs with polymer-ceramic composite matrices enhances ionic conductivity and Li^+ transference number, improving battery performance [24]. Tsurumaki et al. showed that ILs incorporated with inorganic ceramic electrolytes improve ionic conductivity and interfacial stability [25]. However, ionogel electrolytes often face inherent trade-offs in mechanical strength, ion-transport efficiency, and interfacial stability, particularly when high IL contents are required to achieve sufficient room-temperature ionic conductivity [26]. Excessive liquid fractions can compromise dimensional stability and reduce mechanical resistance against lithium dendrite growth, limiting their practical applicability.

To further regulate ion transport and mechanical properties in ionogel electrolytes, inorganic ceramic fillers have been extensively investigated. Chen and colleagues reported that the introduction of ceramic phases can give rise to distinct lithium-ion transport pathways when ceramic particles form percolating networks within the electrolyte matrix [27], consistent with findings reported by Keller et al. [28] Among various ceramic fillers, garnet-type LLZO is particularly attractive due to its high lithium-ion conductivity, wide electrochemical stability window, and single-ion conduction character [29, 30]. To enhance electrolyte performance, both composition and processing strategies have been explored. For example, Ranque et al. modified LLZO particle surfaces to achieve more uniform dispersion within the polymer matrix [31], while Falco et al. employed UV-crosslinking to enhance mechanical integrity [32]. These studies highlight the importance of both compositional and processing control in the development of durable hybrid electrolytes with suitable ionic conductivity and cycling stability. Our previous work demonstrated improved room-temperature cycling stability upon incorporation of LLZO microparticles and suggested a tentative influence of ionic liquid viscosity on the thermal and electrochemical properties of composite systems [33]. Additionally, LLZO has been reported to increase the lithium-ion transference number, improving electrochemical efficiency by mitigating concentration polarization [34–38]. Collectively, these studies emphasize that LLZO material actively complements the polymer-IL phase.

Importantly, although ionogel systems have been increasingly studied, correlations between the component chemistry, such as different ionic liquid local environments, and the resulting macroscopic electrolyte properties for realistic battery applications remain an important area for further investigation [39]. This gap highlights the need to examine how solvation environments influence electrochemical behavior and battery performance at room temperature within carefully designed hybrid matrices. Building on this, we design and investigate hybrid ionogel (HIG) electrolyte membranes obtained by encompassing ionic liquid electrolyte (ILE) solutions in a polymer-in-LLZO host matrix. Our approach is specifically engineered to combine the reported ionic conductivity and thermal robustness of LLZO ceramic nanoparticles with the mechanical integrity and ion-transport enhancement provided by the gel matrix [19, 40–42]. This work focuses on improving the practical application of hybrid solid-state electrolytes by addressing both formulation and processing. Specifically, we fabricate self-standing, ceramic-rich LLZO-based HIG membranes with minimal polymer content using an in situ, solvent-free thermal-polymerization method. This approach includes a direct electrolyte polymerization process on cathode surfaces to facilitate interfacial contact, as examined by cross-sectional FESEM/EDX analysis. In addition, we compare ionic liquid electrolytes featuring single- and mixed-anion environments ($TFSI^-$ and/or FSI^-) to assess formulation-dependent differences in electrochemical behavior. Raman spectroscopy is employed to provide information on anion-related influence on Li^+ coordination and solvation structure. Rather than reiterating the well-established properties of LLZO or ionic liquids in isolation, this work focuses on their combined behavior within ceramic-rich hybrid ionogel systems, providing comparative and experimentally grounded insights relevant to the design of practical solid-state battery electrolytes.

2 | Experimental Section

2.1 | Materials

The raw materials purchased from Sigma–Aldrich include bisphenol A ethoxylate dimethacrylate (BEMA, Mn ~ 1700, EO/phenol: 15) and azobisisobutyronitrile (AIBN). 1-Ethyl-3-methylimidazolium bis(trifluoromethanesulfonyl)imide (EMITFSI), 1-ethyl-3-methylimidazolium bis(fluorosulfonyl) imide (EMIFSI), lithium bis(trifluoromethanesulfonyl)imide (LiTFSI), and lithium bis(fluorosulfonyl)imide (LiFSI, battery grade) were purchased from Solvionic, and Al-doped LLZO nanoparticles (500 nm) from MSE Supplies. The thermal initiator AIBN was recrystallized using methanol to enhance its purity before use, ensuring consistent solubility and distribution in the reaction medium, while other chemicals were used as received.

2.2 | Formulations and Sample Preparation

It is expected that in many liquid-based battery electrolytes, the ionic conductivity has the maximum value at some intermediate salt concentration, which can grant a balance between the number of charge carriers (increased by the increase of salt concentration), the formation of ion pairing that occurs at higher concentrations, and the increase of the viscosity due to increased salt concentration [43]; however, it is a more complex situation when ionic liquids are involved due to the coordination nature in ILs [44]. In this study, different 1 M salt-in-IL electrolyte solutions (ILEs) were prepared for obtaining HIG formulations, of which the salt weight concentration is similar to that of our previously reported LLZO-based hybrid electrolyte [33]. The mixed-anion systems were selected with the aim of leveraging the complementary properties of the two commonly used anions of $TFSI^-$ and FSI^-, for which the hypothesis has been preliminarily explored in multiple studies [45–49]. It is well known that $TFSI^-$ contributes to good chemical, electrochemical, and thermal stabilities of electrolyte performance and good salt dissociation; while FSI^- is considered to provide lower viscosity and better ion diffusivity in the battery cells, as well as to facilitate the formation of a fluorine-rich interphase that improves interfacial stability [17, 48, 50]. Besides, imidazolium-based ILs are found to be very popular for battery applications due to their high chemical stability, low viscosity, and high ionic conductivity [51–53]. These ILEs were mixed with a crosslinker and LLZO ceramic nanoparticles, and such precursors were polymerized via an insitu solvent-free thermal-induced procedure, yielding four hybrid ionogel formulations, namely HIG-TLiT (BEMA + LLZO + EMITFSI + LiTFSI), HIG-TLiF (BEMA + LLZO + EMITFSI + LiFSI), HIG-FLiT (BEMA + LLZO + EMIFSI + LiTFSI), and HIG-FLiF (BEMA + LLZO + EMIFSI + LiFSI). Chemicals used for sample preparation are shown in Scheme 1, and the formulation details of these electrolytes are summarized in Table 1.

First, a specific volume ratio was established for each component (BEMA, ILE, and LLZO), ensuring consistency across all hybrid electrolyte formulations. To prepare the precursors, the thermal initiator AIBN was dissolved in the ILEs at 2 wt% relative to the total formulation mass. Next, the crosslinker BEMA and the inorganic filler LLZO particles were sequentially added and mixed into the solution, following a calculated mass ratio based on their densities and the predefined volume ratio. Accordingly, the final addition sequence was as follows: ILE, AIBN, BEMA crosslinker, and LLZO nanoparticles. Finally, the self-standing HIG electrolyte films were synthesized via an in situ, solvent-free process at 50°C overnight, followed by heating at 60°C for several hours to ensure complete reaction.

2.3 | Materials Characterization

The morphology of HIG series of electrolytes was studied by field emission scanning electron microscopy (FE-SEM). The samples were dipped in liquid nitrogen to crack them while properly preserving their morphology to obtain cross-sectional images. SEM images were subsequently captured using a ZEISS Supra 40VP instrument, operating at an accelerating voltage of 15 kV, to obtain high-quality micrographs for accurate analysis. EDS was also performed on the surface and on the cross-sectional areas of some samples that were directly in situ polymerized on the cathodes. Platinum was used in this study to metallize the sample.

Attenuated total reflectance Fourier-transform infrared (ATR-FTIR) spectra were recorded with a Nicolet iS50 spectrometer to study the surface chemistry, and the Thermo Scientific OMNIC Specta Software was used to record and process the data.

Thermogravimetric analysis (TGA) was conducted to provide information on dehydration, degradation, breakdown, and other chemical reactions that HIGs undergo as a function of temperature; each HIG sample was tested by TG 209 F3 Tarsus Thermogravimetric Analyzer (NETZSCH Gerätebau GmbH), placed in the alumina crucible, under a N_2 flow with a heating rate of 10°C min^{-1}.

Raman characterization of the electrolyte samples was utilized for the ionic interactions and local coordination within HIG electrolyte systems. Raman spectra were collected using a Renishaw inVia (H43662 model, Gloucestershire, UK) equipped with a NIR laser line (785 nm) with a 50× objective. Spectra were recorded in the range from 680 to 790 cm^{-1} with 50 acquisitions and a power of

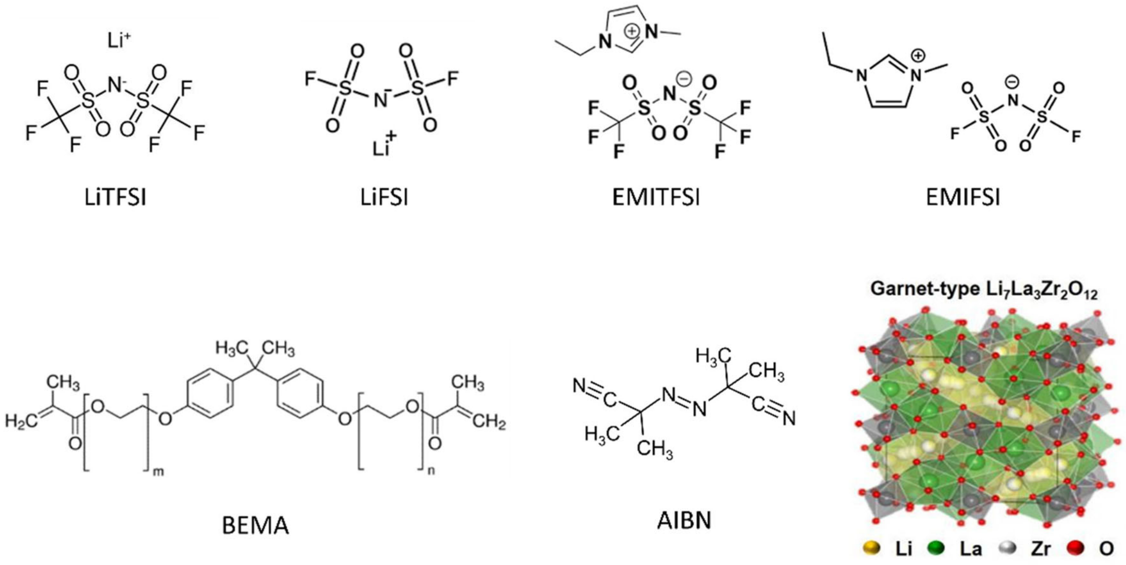

SCHEME 1 | Chemical structures of chemical precursors used for preparing electrolyte samples presented in this study, including reprinted crystal structure of cubic garnet-type LLZO [54].

TABLE 1 | Formulations of the HIGs under study.

	Crosslinker		LLZO particles		ILE, 1M	
Formulations	**vol%**	**wt%**	**vol%**	**wt%**	**vol%**	**wt%**
HIG-TLiT	16	8.65	16	40.00	68	51.35
HIG-TLiF	16	8.69	16	40.15	68	51.16
HIG-FLiT	16	8.80	16	40.66	68	50.54
HIG-FLiF	16	8.84	16	40.86	68	50.30

2.5 mW. Spectra baselines were performed with a script developed using Matlab (version R2020a) [55]. Signals were fitted using Gaussian and Voigt functions, as reported by Kerner et al. [56].

X-ray photoelectron spectroscopy (XPS) was carried out by a PHI 5000 VersaProbe instrument from ULVAC-PHI (Physical Electronics Inc., Kanagawa, Japan) to examine the chemistry change of the surface of HIG-FLiT membrane before and after the CV measurement with carbon-coated Al. The instrument used monochromatic Al Kα radiation with an energy of 1486.6 eV as the X-ray source. Two distinct pass energy values were applied, with 187.75 and 23.5 eV for the survey and the high-resolution spectra, respectively. Throughout the measurements, charge compensation was achieved through a combination of an electron beam and a low-energy Ar beam system.

2.4 | Electrochemical Characterization

A series of electrochemical measurements were performed through laboratory-scale test cells (model ECC-Std by EL-CELL, Germany), and all cells were assembled under the controlled atmosphere of an Ar-filled dry glove-box (MBraun UniLab, H_2O and $O_2 < 1$ ppm). A climatic chamber (Binder MK53 E2) was used to control the operational temperature of the cells accurately.

For ionic conductivity tests, each electrolyte membrane was placed between two identical stainless-steel (SS-316) blocking electrodes, and impedance spectra were recorded by applying an amplitude AC sinusoidal potential of 20 mV in a frequency range of 1 MHz - 100 mHz, and the corresponding impedance was recorded through a VMP-3 electrochemical workstation (BioLogic Science Instruments, France). Cells assembled with disc-shaped HIG membranes were tested at different temperatures, ranging from −20 to 80°C (10°C temperature step). The obtained Nyquist plots were utilized to evaluate the bulk ionic resistance (R) of the electrolyte sample, represented by the amplitude of the semicircle or the intersection of the axis of the real impedance part. The ionic conductivity (σ) of the sample can be subsequently calculated using the formula, where l and A are the thickness and the cross-sectional area of the sample, respectively:

$$\sigma = \frac{l}{\mathrm{A} \cdot \mathrm{R}}$$

Cyclic voltammetry (CV) was conducted to assess the anodic stability behaviors of HIG electrolyte membranes within a voltage range of 2–5 V versus Li^+/Li. The measurements were performed on the Biologic VMP-3 electrochemical workstation at 25°C, utilizing a Li/electrolyte/carbon-coated Al cell configuration. A slow scan rate of 0.1 mV s^{-1} was employed to enable the detection of any oxidation processes [32].

Electrochemical impedance spectroscopy (EIS) experiments were carried out using a Li | Li symmetrical cell configuration to investigate the interfacial properties of HIG electrolytes with Li metal electrodes. Cells were maintained at a constant temperature of 25°C and connected to the BioLogic VMP-3 electrochemical workstation, and the change in resistance over time was measured and recorded. The plotted data illustrates the behavior up to the point where the impedance plateaus, indicating stabilized cell performance. This cutoff was selected to enhance clarity, as the subsequent Nyquist curves became nearly identical and largely overlapped, providing limited additional insight.

Charge/discharge cycling with $LiFePO_4$ (LFP) cathodes was carried out at various current rates with an Arbin BT-2000 battery tester under ambient conditions, corresponding to a measured laboratory temperature of ~21°C. This temperature value was used and given because the point of the study was to estimate the electrolytes and cell behavior in normal room temperature circumstances. The test was performed in the voltage range between 2.6 and 4.0 V versus Li^+/Li for the Li/LFP cells. The current regimes were based on the LFP active material mass loading, derived from the theoretical specific capacity of the active material (170 mAh g^{-1} for LFP). LFP cathode film was prepared from a slurry formulation of LFP, carbon black (Imerys C65), and polyvinylidene difluoride (PVdF, Solvay Solef 6020; dissolved in NMP, Sigma–Aldrich) in a weight ratio of 80:10:10. A relatively low mass loading of 1 mg cm^{-2} was used to achieve better interfacial contact between the solid-state electrolytes and the porous cathode [32]. In addition, HIG precursors were applied to the surface of dried cathodes with a doctor blade before polymerization which aimed to reduce the electrolyte thickness and enhance the penetration of the electrolyte throughout the electrode bulk, optimizing the utilization of active materials. Afterward, electrodes were vacuumed for 15–20 min at 1 Pa in the glovebox antechamber, followed by a thermal curing process to in situ solidify the hybrid electrolyte precursors. The resulting electrodes, conformally coated with the polymer-based HIGs, were then contacted with lithium-metal electrodes and assembled in laboratory-scale cells for cycling tests.

Under the same temperature condition as described above, the Li | Li symmetrical cell configuration was also used for lithium plating/stripping tests to evaluate the durability and operational lifespan of solid-state batteries with our HIG-FLiT electrolyte system. The test was performed by applying a current density of 25 μA cm^{-2} for 4 h during each stripping or plating phase, followed by 50 μA cm^{-2} for 2 h for each subsequent phase, to assess the resistance of the cell to lithium dendrite nucleation and growth, which is a helpful factor in determining safety and longevity [57].

3 | Results and Discussion

3.1 | Characteristics of HIGs

Digital photographs of the fabricated hybrid membranes are shown in Figure 1a–c. After the thermal polymerization process in a stainless-steel mold (Figure 1a), white, self-standing, and ceramic-rich solid-state membranes (~180 µm thick) were obtained. Figure 1b,c shows that the membrane exhibited good mechanical integrity as it withstood multiple folding and releasing cycles without any breaks. The hybrid electrolyte membranes were then cut into smaller disks with a lab-use puncher for different characterization measurements. In addition, the same polymerization method was used to prepare much thicker samples but with a deeper silicone mold for ionic conductivity tests.

The FESEM images of the HIG membranes are shown in Figure 1d–g to provide information on the dispersion of ceramic fillers and the structural quality of the membranes. It is well known that ceramic particles naturally sediment in a liquid-like medium [58] and that the electrochemical properties of LLZO and ionogels toward electrodes differ if phase separation occurs; thus, morphologies on both top and bottom sides of the samples were collected. In general, the top and bottom surfaces of each formulation exhibit similar morphological features; therefore, only the top-view FESEM images are presented here, while the corresponding bottom-surface images are provided in Figure S1. In addition, the Al-LLZO nanoparticles are not very homogenously distributed in the samples. The grain size ranged from tens to thousands of nm in diameter, with occasional aggregates. EMITFSI-based samples (Figure 1d,e) demonstrated more uniform and consistent dispersion characteristics accompanied by reduced agglomeration, compared with EMIFSI-based samples (Figure 1f,g). These differences are likely due to varying combinations of system viscosities and polymerization rates influenced by the formulations, which will not be further discussed here.

The ATR-FTIR spectra for the four polymerized samples are shown in Figure S2 to demonstrate their chemical compositions through vibrational characteristics. It is obvious that all the formulations show at around 3166 and 1572 cm^{-1} the C–H and C–N stretching vibrations, respectively, characteristic of the imidazolium cation ring of EMI-ILs, and the C=O stretching vibration of methacrylate in the range of 1700–1720 cm^{-1}[33]. The spectra for the HIG-TLiT exhibit significant S=O asymmetric stretching vibrations around 1300–1370 cm^{-1} [24]; however, with increasing loading of FSI^- anion, another S=O stretching peak at approximately 1377 cm^{-1} starts to appear and become pronounced, which is considered to be characteristic of the FSI^- anion [59]. The samples containing both anions (HIG-FLiT and HIG-FLiF) suggest a coupling effect of S=O vibrations from $TFSI^-$ and FSI^-, with observed overlaps. Additionally, as the concentration of the FSI anion increases in the HIG samples, the C—SO_2—N bonding mode of $TFSI^-$ in the 1025–1075 cm^{-1} range diminishes; eventually, it disappears in the sample containing only the FSI anion, with which the C—O—C stretching signal around 1100 cm^{-1}[59], being previously overlapped or hidden, becomes noticeable. A similar phenomenon is observed for the S-N stretching vibrations in the 700–860 cm^{-1} range [60]; the peak corresponding to the C-S group in $TFSI^-$ decreases from sample HIG-TLiF to HIG-FLiT and then to HIG-FLiF. These spectral differences demonstrate distinct chemical environments fostered by FSI and TFSI anions. It should be noted that the peaks show discrepancy compared with pure components, as the specific anionic compositions as well as the integrated polymer matrix and ceramic particles influence the overall vibrational profile of the samples.

TGA is included to confirm the thermal integrity of the hybrid electrolyte systems and to support the soundness of our formulation strategy. The plotted curves of the four samples are shown in Figure 2 revealing their thermal degradation profiles, which exhibit good thermal stability up to the breakdown temperature at around 280°C or 380°C with FSI-IL or TFSI-IL, respectively. Gradual mass losses at lower temperatures are likely ascribable to the evaporation of absorbed moisture and crystallization water; indeed, samples were stored in ambient air before TGA testing, and all chemicals were used as purchased without any pretreatment. The main degradation events occur approximately between 300°C and 500°C, which can be ascribed to the decomposition of the polymer matrix and associated ionic species. The EMITFSI-based samples are more stable than the EMIFSI-based ones, which should be attributed to the stronger interactions between EMI^+ and $TFSI^-$ [46]. Additionally, increasing the concentration of FSI^- generally lowers the thermal stability, and among the samples, HIG-FLiF (blue) shows the most significant

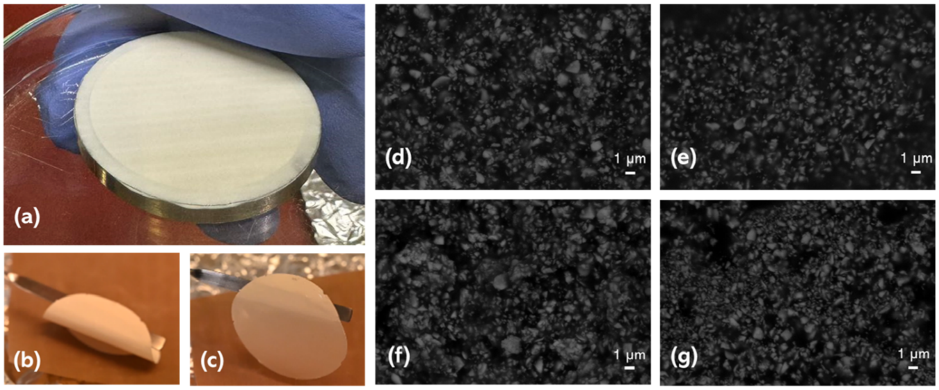

FIGURE 1 | Digital photographs showing the thermal-polymerized HIG sample in ~180 µm thickness (a) in a stainless-steel mold, (b) folded after being peeled off from the mold, and (c) released, demonstrating self-standing integrity and ease of handling. FESEM images of the HIG series of electrolyte membranes under study: top views of (d) HIG-TLiT, (e) HIG-TLiF, (f) HIG-FLiT, and (g) HIG-FLiF.

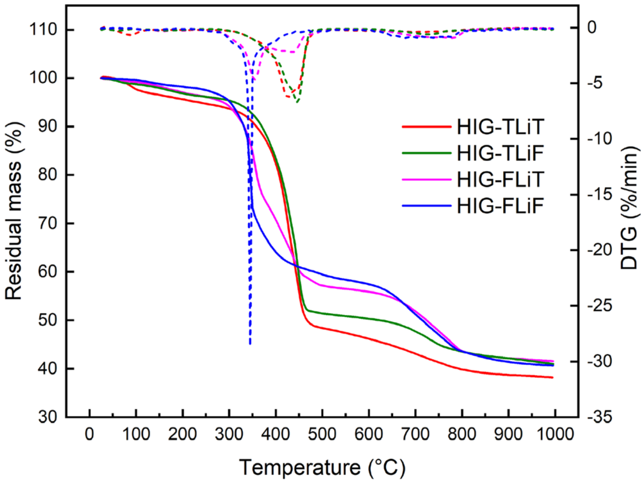

FIGURE 2 | TGA traces of electrolyte membranes under study: HIG-TLiT (red), HIG-TLiF (green), HIG-FLiT (magenta), and HIG-FLiF (blue) and their derivative weight vs. temperature plots.

mass loss, starting at around 300°C and continuing more steeply compared to the others, suggesting a less thermally stable system. In contrast, HIG-TLiT (red) and HIG-TLiF (green) show more gradual degradation profiles, indicating relatively higher thermal stability contributed by EMITFSI ionic liquid. The derivative thermogravimetry (DTG) curves further highlight these differences, with peaks indicating the maximum rate of mass loss. Furthermore, the HIG-FLiT (magenta) shows two-step decomposition behavior between 300°C and 500°C that indicates more complex degradation processes. Conversely, the HIG-TLiF sample, which also contains both TFSI and FSI anions, does not show two distinct peaks in the DTG curve in the same decomposition range. This phenomenon could be attributed to the polymer structure discrepancy caused by the viscosities of reaction media [33].

The superimposed Raman spectra of all the samples are shown in Figure 3. For a detailed discussion, the deconvolved spectra of each sample are presented; the corresponding fitting results are summarized in Table 2. A peak at around 701–702 cm^{-1} is observed in all samples and is assigned to the EMI cation. The limited shifts in peak position (701 cm^{-1} in HIG-TLiT/TLiF, Figure 3b,c, and 702 cm^{-1} in HIG-FLiT/FLiF, Figure 3d,e) reflect slight differences in the local environment, likely arising from different ionic liquid anions. The spectra of HIG-TLiT and HIG-TLiF in Figure 3b,c exhibit similar features with four components. The peak at 733 cm^{-1} is attributed to the presence of the TFSI anion, while the much stronger signal at about 742 cm^{-1} corresponds to the dominant Raman-active mode of $TFSI^{-}$. The occurrence of these two "free-TFSI" features is consistent with previous reports on ionic liquid systems [46] and is associated with the different local environments and cis/trans conformers of uncoordinated $TFSI^{-}$ in EMITFSI-based systems. The slight differences in relative peak areas are attributed to baseline variations and fitting uncertainty, and the two spectra are therefore considered not significantly different. In analogy with TFSI-rich systems, EMIFSI-based samples display peaks at 725 and 726 cm^{-1} in HIG-FLiF (Figure 3d) and HIG-FLiT (Figure 3e) respectively, which are characteristic of the uncoordinated form of FSI^{-}. In addition, the HIG-FLiT formulation shows both features of TFSI and FSI anions with an approximate ratio of 2:5, and the spectrum was fitted with Voigt functions and did not require any additional unassigned peaks. Furthermore, the peak centered at 749 cm^{-1} in the spectra of TFSI-rich samples is attributed to the formation of $[Li(TFSI)_x]^{-(x-1)}$ coordination complexes, as reported in literature [61]. The relatively weak band observed at around 740 cm^{-1} in the HIG-FLiF spectrum can similarly be assigned to the presence of $[Li(FSI)_x]^{-(x-1)}$ complexes [46].

Figure S3 shows the temperature dependence of the ionic conductivity for HIG-TLiT, HIG-TLiF, HIG-FLiT, and HIG-FLiF samples from −20°C to 80°C during the heating step and back to −20°C during cooling. All samples show increasing ionic conductivity with temperature, characteristic of thermally activated ionic conduction. Furthermore, similar or nearly identical conductivity values are observed during heating and cooling cycles, indicating good thermal reversibility. This consistency suggests that the incorporation of LLZO ceramic particles contributes to the stability of ionic transport across the investigated temperature range, likely by maintaining the structural integrity of the hybrid membranes and mitigating conductivity fluctuations associated with polymer relaxation or phase redistribution during heating [62, 63]. As heating curves are generally more relevant for practical applications [64], Figure 4 compares the ionic conductivity of the four hybrid solid electrolytes upon heating from −20°C to 80°C. HIG-FLiT exhibits the highest ionic conductivity (1.93×10^{-3} S cm^{-1} at 20°C), followed by HIG-FLiF, while HIG-TLiF and HIG-TLiT show slightly lower values, with the latter providing the lowest ionic conductivity (1.75×10^{-3} S cm^{-1} at 20°C) in the series. Although the absolute differences are modest, a consistent formulation-dependent trend has been observed, with the FSI-rich systems exhibiting higher ionic conductivities across the entire investigated temperature range. This trend is consistent with Raman spectral analysis (Table 2), which reveals relative differences in the contributions of uncoordinated and coordinated anion-related features among the samples. The findings are in agreement with existing literature in which a higher proportion of "free" anions has often been associated with increased ionic conductivity in ionic-liquid-based electrolytes, emphasizing the role of local solvation and the coordination environment imposed by different ionic liquids [65, 66].

In particular, the superior conductivity of HIG-FLiT suggests that the combination of LiTFSI and EMIFSI, together with the LLZO filler and polymer matrix, promotes enhanced ionic mobility. The weakly coordinated $TFSI^{-}$ originating from the lithium salt are expected to exhibit higher mobility and thus contribute significantly to ionic transport, in agreement with previous studies on anion coordination effects in ionic-liquid-based electrolytes [45, 46, 67]. While the dominant contribution to conductivity arises from the ionogel phase, the presence of high-surface-area LLZO ceramic particles may additionally influence the local ionic environment, as reported for inorganic-filler-containing quasi-solid electrolytes where ceramic-ion interactions have been suggested to affect ion dynamics [63, 68, 69]. An empirical analysis of the temperature dependence of ionic conductivity was additionally performed using a Vogel–Tammann–Fulcher (VTF) model expressed in $\ln(\sigma)$ space; the corresponding results are provided in the Supporting Information.

In the analysis of lithium metal compatibility with the HIG electrolytes, Nyquist plots are shown in Figure 5 to illustrate the areal impedance spectra of Li | Li cells assembled with four different formulations over various time intervals at 25°C. Despite the preparation method showing inherent variability, which results in slight differences in sample thickness, thus affecting impedance values, all four formulations reach a stabilization phase where the

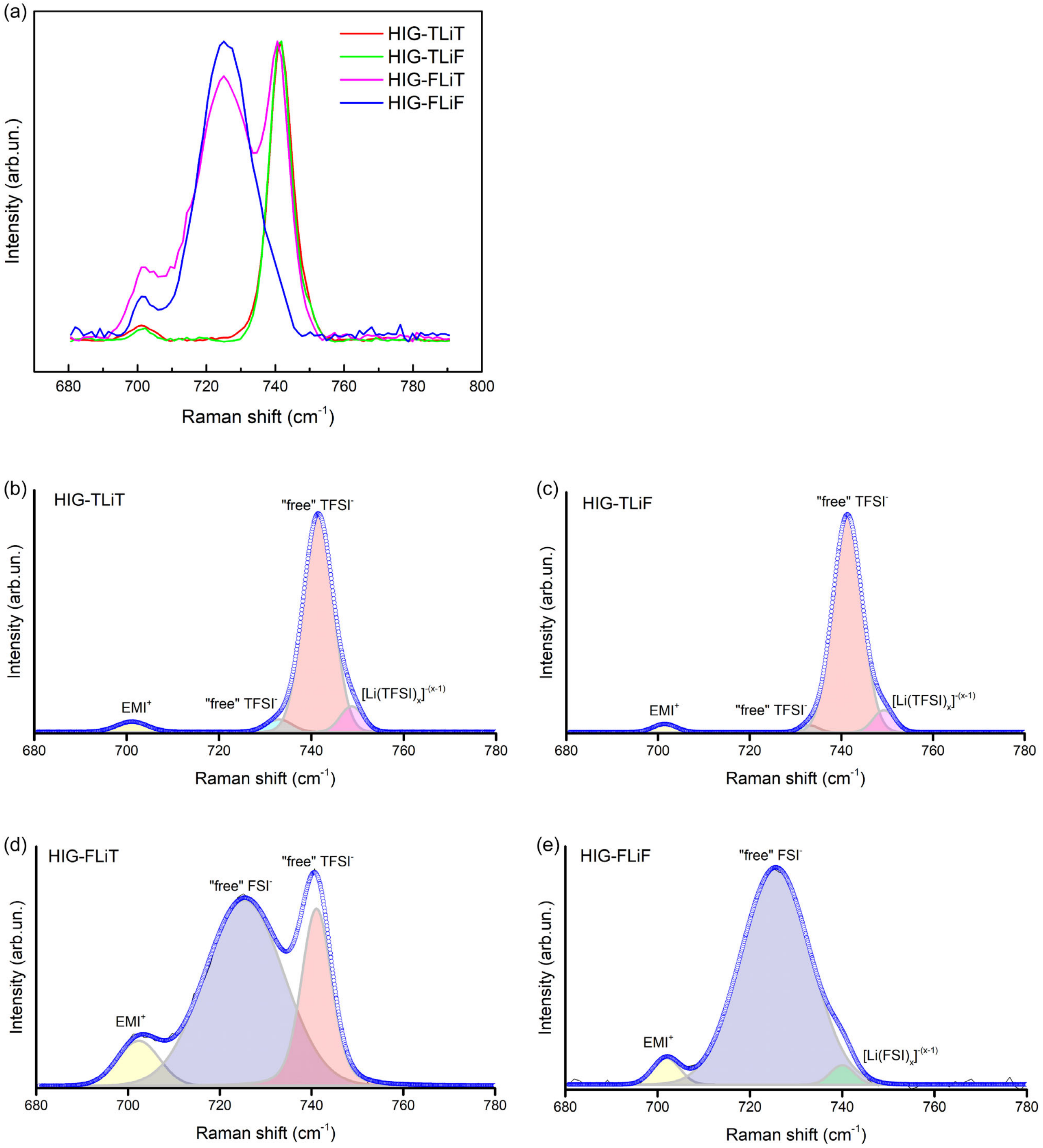

FIGURE 3 | (a) Raman spectra in the range from 680 to 790 cm^{-1} of the HIG series of samples under study and fitted Raman spectra of (b) HIG-TLiT, (c) HIG-TLiF, (d) HIG-FLiT, and (e) HIG-FLiF.

electrolyte structures optimize for ion transport. Initially, the HIG-TLiT formulation (Figure 5a) displays an increase in areal impedance within 1 day, followed by a gradual decrease until around the 6th day when it stabilizes, indicating a slow but steady reorganization of the electrolyte structure. On the other hand, HIG-TLiF (Figure 5b) exhibits an initial rise and gradual change in areal impedance over time, eventually stabilizing after 15 days. As this sample had not reached stabilization within the earlier period compared with others, it was monitored for a longer duration. Among all samples, it took the most time to undergo substantial structural reorganization. Moving to EMIFSI-based samples, HIG-FLiT (Figure 5c) shows a rapid decrease in areal impedance, reaching equilibrium within 2 days, which is the shortest time frame among all the samples, suggesting a remarkable interface stability [70, 71]. HIG-FLiF (Figure 5d) demonstrates a relatively quick decrease in areal impedance, stabilizing within around 6 days. A second semicircle appears in the spectrum of the HIG-TLiT system after a couple of days, which can correspond to the grain boundary. However, other HIG formulations do not exhibit the same phenomenon, potentially due to the existence of FSI$^-$ which might improve dispersion and interaction of LLZO with the polymer matrix, resulting in more uniform ionic channels and reduced grain boundary

TABLE 2 | Output of Raman analysis of the HIG series of samples under study.

Formulation	Components	Center, cm^{-1}	Area, %
HIG-TLiT	EMI^+	701	4.1
	"free" $TFSI^-$	733	4.2
	"free" $TFSI^-$	742	84.2
	$[Li(TFSI)_x]^{-(x-1)}$	749	7.5
HIG-TLiF	EMI^+	701	2.7
	"free" $TFSI^-$	733	1.8
	"free" $TFSI^-$	741	88.9
	$[Li(TFSI)_x]^{-(x-1)}$	749	6.6
HIG-FLiT	EMI^+	702	8.4
	"free" FSI^-	725	65.2
	"free" $TFSI^-$	741	26.4
HIG-FLiF	EMI^+	702	4.4
	"free" FSI^-	726	92.7
	$[Li(FSI)_x]^{-(x-1)}$	740	2.9

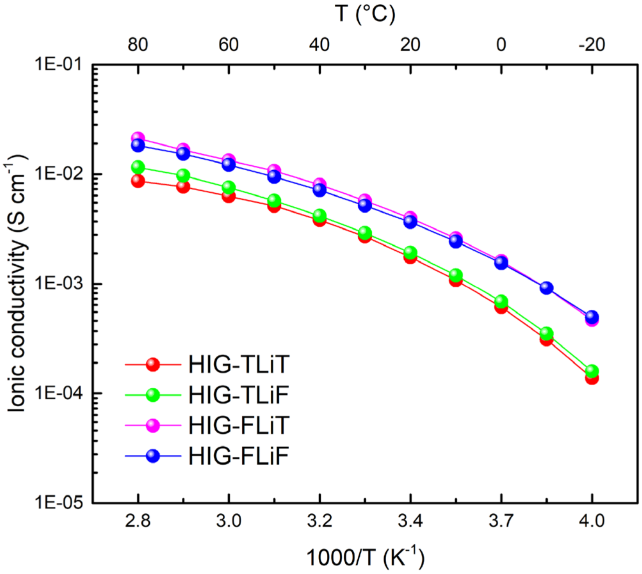

FIGURE 4 | Comparison of the ionic conductivity results for the samples HIG-TLiT, HIG-TLiF, HIG-FLiT, and HIG-FLiF upon heating from −20 to 80°C. Corresponding heating-cooling data are shown in Supporting Information.

resistance. The underlying mechanism for this behavior is still under investigation and is beyond the scope of this work. However, for all four electrolyte formulations, as indicated by the impedance values, the effective interfacial contact at the electrode surfaces remains challenging, likely due to the poor wettability between solid/solid surfaces and the low degree of uniform dispersion of LLZO particles.

With the same lithium symmetric cell configuration, stripping-plating experiments were conducted on the HIG-FLiT formulation at room temperature, and the corresponding voltage response is shown in Figure S5. The cell was cycled for approximately 100 h, during which the ∼180 μm thick electrolyte membrane exhibited stable operation without short-circuiting. The overpotential increased gradually from around 0.5–0.75 V at 25 μA cm^{-2} and rose further at 50 μA cm^{-2}. This behavior is consistent with expectations for relatively thick, ceramic-rich hybrid membranes, where large interfacial resistance and slower charge–transfer processes contribute to increased polarization [72–74], as also reflected in the impedance measurements (Figure 5). Importantly, the absence of short-circuiting throughout the 100-hour test suggests stable interfacial behavior and effective suppression of dendrite growth at low current density for operating solid-state battery applications at room temperature conditions, while also highlighting the need for further optimization of membrane thickness, processing, and interfacial contact to reduce the resistance and polarization.

The cyclic voltammograms were performed across the four HIG formulations, as well as to demonstrate the general electrochemical robustness and stability of the materials that may support any future application with high-voltage cathodes. The current response to voltage is represented in each plot across several cycles. The formulation of HIG-FLiT (Figure 6) demonstrates the highest onset decomposition potential among the four electrolyte systems [75], and, therefore, it is electrochemically stable enough to be coupled with $LiFePO_4$-based cathodes in Li-metal cells [76]. Other HIGs, as plotted in Figure S6a–c, do not perform at the same level; they show more pronounced minor oxidation features, and this behavior is attributed to formulation-dependent differences in the ionic environment and interfacial reactions [45]. Although sharing the same ionic liquid as in HIG-FLiT, HIG-FLiF (Figure S6c) exhibits the lowest breakdown voltage among the four electrolytes, suggesting less stability of FSI anion [46, 49]. In general, the more obvious current flows in the first cycle can be associated with the decomposition of impurities and formation of side products; nevertheless, over the following cycles, most peaks become less intense, even disappearing, indicating the conversion of those side products. Overall, the presence of both TFSI and FSI anions is advantageous for anodic stability. The ionic liquid electrolytes predominantly influence the CV behavior of the samples; however, LLZO as an electrochemically stable, structurally reinforcing phase whose microstructural distribution can also influence interfacial behavior [77].

To evaluate their practical electrochemical performance, HIG electrolytes were *in* situ polymerized onto the LFP cathodes (active material mass loading: 1 mg cm^{-2}) as detailed earlier and directly assembled in laboratory-scale cells against lithium metal for constant current charge–discharge tests at room temperature. The resulting in situ polymerized solid electrolyte layer had an average thickness of approximately 75 μm, which is substantially thinner than the free-standing membranes (∼180 μm) used for other characterizations, as enabled by the in situ polymerization strategy. Different constant current rates (at C/20, C/10, and C/5, based on the LFP active material mass in the electrode disk) were applied to the cells until the voltage reached a predefined cutoff value (4.0 and 2.6 V vs. Li^+/Li for charge and discharge, respectively), where the controller switches to the constant voltage mode, holding the voltage at 4.0 or 2.6 V for 3 h unless the current was out of the range of ± 6 μA (limited by the charge–discharge current values at C/50).

The HIG-FLiT-based cell demonstrates the best cyclability and performance among the four formulations, as shown in Figure 7. The cycling result (Figure 7a) shows specific discharge capacities approaching 130 mAh g^{-1} up to C/5 and Coulombic

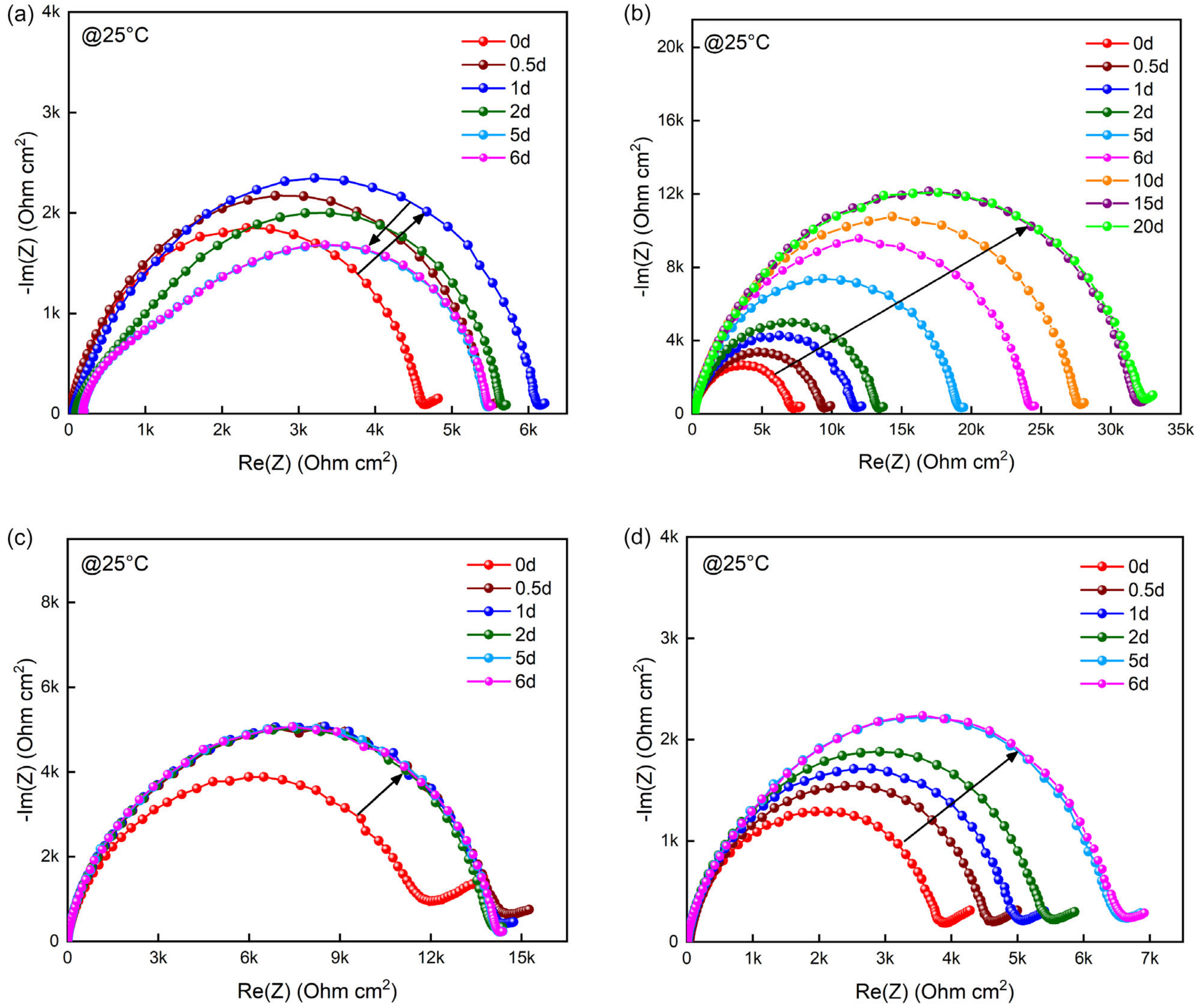

FIGURE 5 | Areal impendence spectroscopy results against time, under OCV at 25°C, for symmetric lithium cells assembled with (a) HIG-TLiT, (b) HIG-TLiF, (c) HIG-FLiT, and (d) HIG-FLiF.

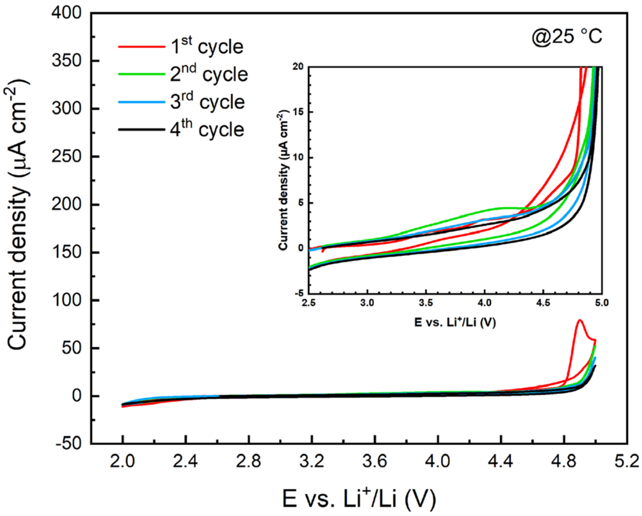

FIGURE 6 | Cyclic voltammetry profiles at a scanning rate of 0.1 mV s^{-1} of Li-metal cell assembled with HIG-FLiT membrane against carbon-coated Al at 25°C, with the inset zoomed-in view.

efficiency above 99.3% except for the initial cycle (96.2%). Figure 7b shows representative voltage versus specific capacity profiles of the first cycle at each different C-rate. Overall, excellent cycling stability was demonstrated by HIG-FLiT with outstanding capacity retention during the whole cycling test, as well as remarkable Coulombic efficiency capacity at different C-rates up to C/5. The specific capacity delivered decreases only slightly while increasing the current regimes from 1st to 16th cycles. The charge/discharge potential profiles versus specific capacity at different current rates perfectly resemble the typical flat plateaus of the LFP cathode corresponding to the Li$^+$ ion insertion (discharge) in the $FePO_4$ network. The observed profiles remained stable even upon doubling the current rate, with overall limited overpotential that only slightly increased at a higher rate of C/5, supporting the favorable charge transport properties of the system. The capacity of cells with HIG-FLiT electrolyte starts declining only when continuously transitioning to 1C and then to higher rates (2C and 5C), as shown in Figure S7a, and does not recover to initial levels upon returning to 1C. The faster decrease at higher rates suggests that this condition

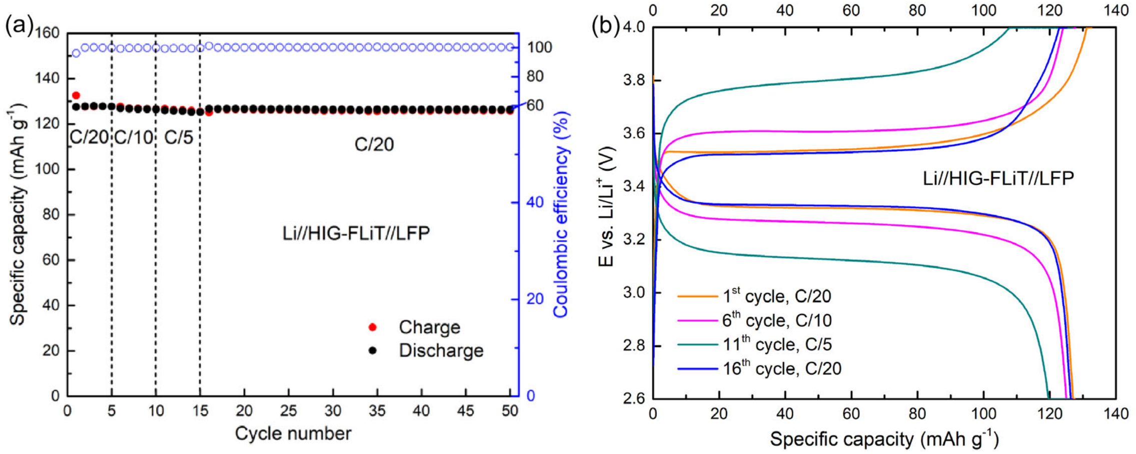

FIGURE 7 | Charge/discharge cycling behavior of (a) HIG-FLiT at the current rates of C/20, C/10, and C/5 and (b) its voltage profile as a function of the specific capacity. The cell tests were conducted at room temperature (~21°C). Current density at 1C: 0.13 mA cm^{-2}. The LFP loading was 1.0 mg cm^{-2}, corresponding to a theoretical areal capacity of 0.17 mAh cm^{-2}.

enhances irreversible degradation phenomena, accompanied by reduced stability of the solid electrolyte interphase layer that increases resistance and decreases active lithium ion availability [78]. As mentioned earlier, the current low areal loading (1.0 mg cm^{-2}) was chosen in order to evaluate intrinsic electrochemical behavior and ensure good contact with the relatively dry, rigid membranes, but increasing the loading for commercial relevance is an acknowledged challenge in solid-state electrolytes and will be a focus of future electrolyte optimization.

Moving to other formulations, HIG-TLiT shows poor cyclability, as plotted in Figure S7b, with a noticeable decay in capacity and Coulombic efficiency over cycles, indicating less favorable cycling stability compared with other formulations. On the other hand, HIG-TLiF (Figure S7c) exhibits stable specific capacities exceeding 130 mAh g^{-1} from C/20 to C/5 with high Coulombic efficiency. Lastly, the cell assembled with HIG-FLiF (Figure S7d) provides high discharge capacities near 145 mAh g^{-1} at C/20 rate, but with poor Coulombic efficiency, likely due to side reactions at the electrode/electrolyte interface. Significantly, both single-anion-based systems (HIG-TLiT and HIG-FLiF) exhibit a propensity to undergo short-circuiting, indicating the possibility of stability issues throughout prolonged cycles. The observations of cell performance employing systems containing both TFSI$^-$ and FSI$^-$ confirmed their combined effect on the cell electrochemical responses, especially with the excellent stability of HIG-FLiT in retaining a high capacity and efficiency. Nonetheless, performance at higher C-rates still requires further development and optimization, particularly with respect to LLZO particle dispersion and interfacial engineering, which may help improve interfacial stability and reduce polarization in ceramic-rich hybrid electrolytes [79]. In addition, these findings highlight the strong influence of the ionic liquid chemistry on electrochemical performance, reflecting differences in viscosity, ionic interactions, and intrinsic electrochemical stability. A summary of the initial specific discharge capacity for HIG electrolytes at different C-rates is shown in Table 3.

3.2 | Further Evaluation of HIG-FLiT

Based on its best overall performance in terms of Raman spectrum, ionic conductivity, compatibility with lithium metal, anodic stability window, and charge–discharge galvanostatic cycling at room temperature, the electrolyte system HIG-FLiT was identified as the most promising candidate and was consequently selected for more detailed investigation. FESEM with EDX was conducted to investigate element distribution on the surface as well as its in situ cross-section onto the cathode electrode. In addition, XPS was applied to the electrolyte membrane surface, contacting carbon-coated Al before and after CV tests to examine the chemical reactions at the interface between the electrolyte and cathode.

Figure 8 shows the EDX maps of the distribution of different elements of the surface of the HIG-FLiT sample (Figure 8a), viz. aluminum (Al), carbon (C), fluorine (F), lanthanum (La), nitrogen (N), oxygen (O), sulfur (S), and zirconium (Zr). The mappings show a relatively homogeneous elemental distribution, with a few noteworthy discoveries. C (Figure 8c), F (Figure 8d), N (Figure 8f), O (Figure 8g), and S (Figure 8h) are equally distributed, showing that the polymer matrix is consistent and the dissolved LiTFSI salt is effectively integrated. Al (Figure 8b), La (Figure 8e) and Zr

TABLE 3 | Summary of the initial specific discharge capacity for HIG electrolytes at different C-rates.

Formulation	Initial capacity, mAh g^{-1} at C/20	Initial capacity, mAh g^{-1} at C/10	Initial capacity, mAh g^{-1} at C/5	Initial capacity, mAh g^{-1} at C/20 2nd
HIG-TLiT	42.5	77.0	53.2	49.9
HIG-TLiF	136.7	136.7	137.5	136.0
HIG-FLiT	127.6	126.9	126.8	125.1
HIG-FLiF	143.7	142.1	138.4	141.4

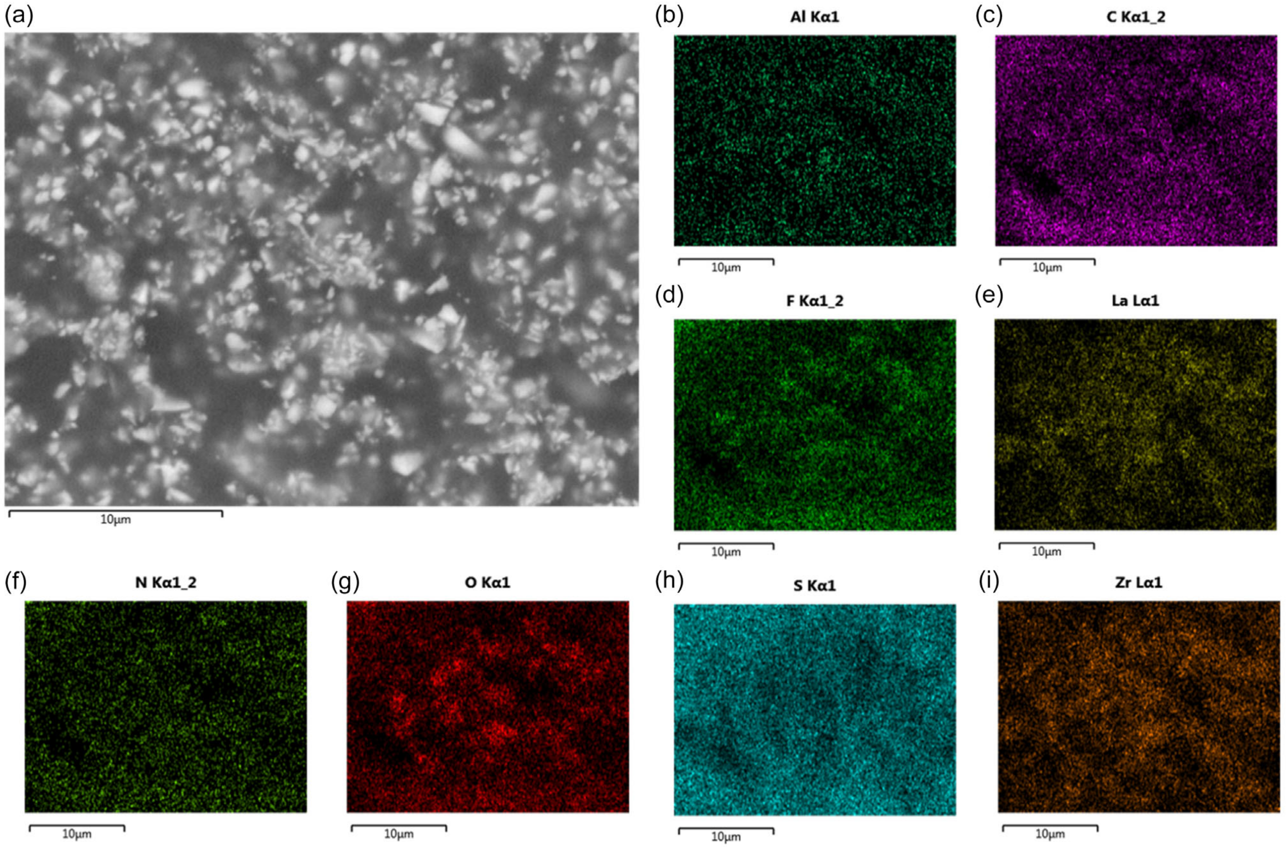

FIGURE 8 | FESEM image of (a) HIG-FLiT electrolyte membrane surface, and EDX mapping images for elements: (b) Al, (c) C, (d) F, (e) La, (f) N, (g) O, (h) S, and (i) Zr.

(Figure 8i), which correspond to Al-doped LLZO particles, are found in more concentrated areas; they also exhibit significant clustering, aligning with FESEM results discussed previously. These findings imply that, while the overall elemental distribution is uniform, ceramic particle agglomeration still occurs, which may impact the interfacial contact with electrodes and, therefore, ion transport and cycling performance of the material.

The in situ approach was employed to polymerize the electrolyte precursor directly onto the cathode surface for the purpose of conducting charge-discharge tests in laboratory-scale cells. To assess the effectiveness of the procedure and the good contact between interfaces allowing excellent specific capacity output, a FESEM cross-sectional analysis was performed on the HIG-FLiT electrolyte membrane polymerized on the LFP cathode (Figure 9). Additionally, FESEM equipped with EDX was used to examine the distribution of elements across the cross section, enabling identification of the electrolyte and cathode regions, assessment of interfacial contact, and evaluation of electrolyte penetration into the porosity of the cathode. Four locations were analyzed. Based on the elemental analysis, spot 1 (Figure S8a)

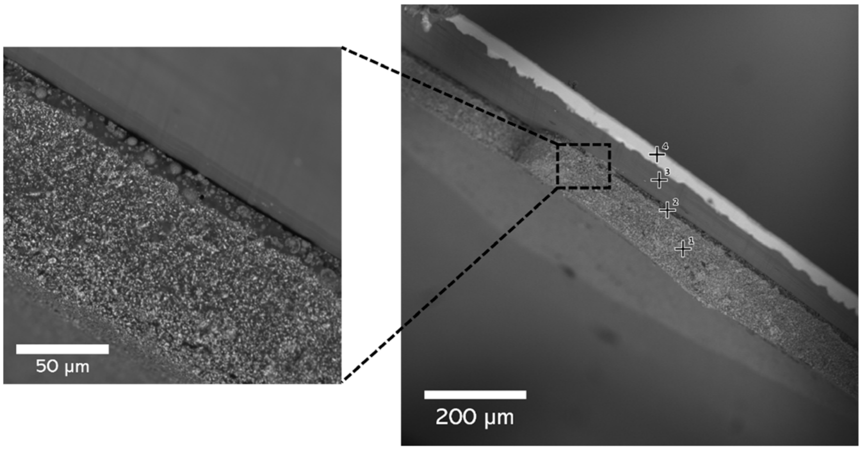

FIGURE 9 | Cross-sectional FESEM image of the HIG-FLiT electrolyte thermally polymerized in situ on the LFP cathode, showing good penetration and intimate physical contact. Complementary elemental spots 1–4 analysis is provided in the Supporting Information.

corresponds to the hybrid electrolyte, whereas spot 2 (Figure S8b), taken from a darker area, exhibits the presence of thin LFP coating layer of the cathode. Furthermore, it indicates in spot 2 the presence of small quantities of fluorine (F), aluminum (Al), sulfur (S), zirconium (Zr), nitrogen (N), and lanthanum (La), suggesting successful partial penetration of the hybrid electrolyte into the cathode structure and intimate interfacial contact. Spots 3 and 4 (Figure S8c,d) correspond to regions within the aluminum current collector.

The XPS spectra of the HIG-FLiT membrane cycled with carbon-coated Al against lithium metal were collected to study the bonding structures of the elements on the surface of the electrolyte membrane before and after CV experiments. Results are shown in Figure S9. Spectra of various elements are shown, including C, O, N, and F, with their XPS output summarized in Table S2. In the C 1s spectrum, the peak at ~284.8 eV associated with carbon in EMI^+ slightly decreases in area from 70.5 to 69.7% [24]. The peak at ~286.0 eV, associated with C─O bonds [80], appears at 286.8 eV post-cycling, and its area increases from 15.7 to 24.1%, indicating increased oxidation. The peak at ~288.5 eV disappears after CV, as a result of some electrochemical reactions occurring. The O 1s spectrum shows a 531.4 eV peak for Li_2O [81], with a minimal shift in position (531.3 eV) and an area increase from 55.6 to 64.1% after CV. The peak at ~287.1 eV is related to C═O bonds [47]; it appears at 287.7 eV after CV and its area decreases from 10.2 to 6.2%. The small peak at ~533.7 eV, attributed to C─O bonds on polymer [82], is detected at 533.8 eV after cycling, and its area reduces from 5.3 to 3.4%. The N 1s spectrum displays four prominent peaks in the range of 395–405 eV with minor changes in position and intensity, indicating changes in nitrogen species due to electrolyte decomposition. It includes the peak at ~398.3 eV for Li_3N [81] that appears at 398.5 eV after CV, with an area increase from 22.1 to 26.5%, as well as the peak at ~399.8 eV from TFSI anion [83], with its area slightly increasing from 39.5 to 43.8%. LiF (684.8 eV in the F 1s spectra) is usually believed to minimize the side reactions between interfaces to increase electrochemical cycling stability [80]. In addition, the Li 1s peak observed in the sample after CV exhibits a reduced binding energy, suggesting the formation of compounds containing lithium [83]. It should be noted that the small "shifts" observed are understood as reflecting variations in the local chemical environment, rather than indicating a complete change in chemical species. Therefore, our discussion focuses primarily on differences in relative peak areas to track the evolution of surface composition. The implications of such surface changes for interfacial stability are discussed in conjunction with the electrochemical results. Together, these observations are consistent with the formation of an interfacial layer during initial electrochemical reactions, which may contribute to the stable anodic behavior and overall cycling performance observed for the HIG-FLiT electrolyte.

4 | Conclusions

This work has successfully developed and thoroughly characterized four ceramic-rich hybrid ionogel electrolytes using a practical in situ and solvent-free fabrication method. Different ILEs as reaction media containing single or binary anion environments and their impact on the properties of the resulting HIG electrolytes were studied by comprehensive electrochemical and spectroscopic analyses. All systems presented high ionic conductivities, with HIG-FLiT (EMIFSI-LiTFSI ILE) outperforming the other formulations. The effect of mixing TFSI and FSI anions was confirmed through Raman analysis and electrochemical characterization including CV, EIS, charge–discharge cycling, and lithium stripping-plating. Our findings highlight the superior performance of HIG-FLiT, which stabilizes quickly and maintains efficient ion transport, making it the most promising formulation in this study for safe, high-energy-density lithium metal batteries. FSI anions in both EMIFSI-based formulations contributed to favorable solvation environments and less complex ion-pairing dynamics, enhancing overall performance. This observation aligns with studies that emphasize the importance of SEI stability and ion transport mechanisms in determining the efficiency of Li-based batteries. In addition, the high cycling stability and coulombic efficiency of HIG-FLiT at room temperature account for its promising prospects, implying a significant contribution to electrolyte technology development. Albeit further improvement and electrolyte optimization in terms of anion environment, more homogeneous LLZO dispersion, and surface/interface engineering are necessary to achieve optimal performance at high current rates, here we offer a path toward solid-state Li-based batteries with better safety, energy density, and operational stability. In general, our in situ and solvent-free fabrication method, ILE compositional design, ceramic-polymer balance, and mechanistic characterization collectively present a novel and practically relevant perspective on hybrid lithium metal electrolytes and a meaningful contribution to the relevant field.

Acknowledgments

This work was supported by the European Union's Horizon 2020 research and innovation program under the Marie Skłodowska-Curie grant agreement no. 860403 (European Training Network POLYSTORAGE https://www.polystorage-etn.eu/). This manuscript reflects only the authors' views and opinions; neither the European Union nor the European Commission can be considered responsible for them. Part of this work was conducted within the activities of "Ricerca Sistema Elettrico" funded through contributions to research and development by the Italian Ministry of Economic Development. Support under the MUR program "Dipartimenti di Eccellenza 2023–2027" (CUPE17G22001490006) is gratefully acknowledged. Y.Z. would like to acknowledge Toyota Motor Europe (TME) and Dr. Laurent Castro for the facilities and guidance, Dr. Hamideh Darjazi (DISAT, Politecnico di Torino) for assistance with XPS plotting, as well as Dr. Camilla Noè (DISAT, Politecnico di Torino) for the support with part of the FESEM measurements.

Open access publishing facilitated by Politecnico di Torino, as part of the Wiley - CRUI-CARE agreement.

Conflicts of Interest

The authors declare no conflicts of interest.

Data Availability Statement

The data supporting this article have been included as part of the Supplementary Information.

References

1. R. A. Huggins, *Energy Storage* (Springer International Publishing AG, 2016), 119–144, Chapter 9, https://10.1007/978-3-319-21239-5_9.

2. K. M. Maraz and D. Ahmed, “Polymer Electrolyte Design Strategies for High-Performance and Safe Lithium-Ion Batteries: Recent Developments and Future Prospects,” *Materials Engineering Research* 5 (2023): 245–255.

3. Z. Gao, H. Sun, L. Fu, et al., “Promises, Challenges, and Recent Progress of Inorganic Solid-State Electrolytes for All-Solid-State Lithium Batteries,” *Advanced Materials* 30 (2018): e1705702.

4. A. Machín, C. Morant, and F. Márquez, “Advancements and Challenges in Solid-State Battery Technology: An In-Depth Review of Solid Electrolytes and Anode Innovations,” *Batteries* 10 (2024): 29.

5. Y. Zheng, Y. Yao, J. Ou, et al., “A Review of Composite Solid-State Electrolytes for Lithium Batteries: Fundamentals, Key Materials and Advanced Structures,” *Chemical Society Reviews* 49 (2020): 8790–8839.

6. L. Fan, S. Wei, S. Li, Q. Li, and Y. Lu, “Recent Progress of the Solid-State Electrolytes for High-Energy Metal-Based Batteries,” *Advanced Energy Materials* 8 (2018): 11.

7. J. Janek and W. G. Zeier, “A Solid Future for Battery Development,” *Nature Energy* 1 (2016): 9.

8. J. Schnell, T. Günther, T. Knoche, et al., “All-Solid-State Lithium-Ion and Lithium Metal Batteries – Paving The Way to Large-Scale Production,” *Journal of Power Sources* 382 (2018): 160–175.

9. A. Ahniyaz, I. de Meatza, A. Kvasha, et al., “Progress in Solid-State High Voltage Lithium-Ion Battery Electrolytes,” *Advances in Applied Energy* 4 (2021): 100070.

10. Q. Zhou, J. Ma, S. Dong, X. Li, and G. Cui, “Intermolecular Chemistry in Solid Polymer Electrolytes for High-Energy-Density Lithium Batteries,” *Advanced Materials* 31 (2019): e1902029.

11. D. Zhou, D. Shanmukaraj, A. Tkacheva, M. Armand, and G. Wang, “Polymer Electrolytes for Lithium-Based Batteries: Advances and Prospects,” *Chem* 5 (2019): 2326–2352.

12. L. Zhong, Z. Li, S. Wang, and S. Huang, “Ultra-Thin Solid Electrolyte in Lithium-Ion Batteries,” *Sustainable Polymer & Energy* 1 (2023): 1–17.

13. J. Yue, M. Yan, Y. X. Yin, and Y. G. Guo, “Progress of the Interface Design in All-Solid-State Li–S Batteries,” *Advanced Functional Materials* 28 (2018): 38.

14. X. Ji, Y. Zhang, M. Cao, et al., “Advanced Inorganic/Polymer Hybrid Electrolytes for All-Solid-State Lithium Batteries,” *Journal of Advanced Ceramics* 11 (2022): 835–861.

15. X. Yu and A. Manthiram, “A Review of Composite Polymer-Ceramic Electrolytes for Lithium Batteries,” *Energy Storage Materials* 34 (2021): 282–300.

16. M. Keller, A. Varzi, and S. Passerini, “Hybrid Electrolytes for Lithium Metal Batteries,” *Journal of Power Sources* 392 (2018): 206–225.

17. X. Tang, S. Lv, K. Jiang, G. Zhou, and X. Liu, “Recent Development of Ionic Liquid-Based Electrolytes in Lithium-Ion Batteries,” *Journal of Power Sources* 542 (2022): 231792.

18. C. Manasa, V. Basavanna, and S. Ningaiah, “Ionic Liquid-Based Hybrid Materials: Ionogel Review,” *Biointerface Research in Applied Chemistry* 13 (2022): 391.

19. Y. Hu, L. Yu, T. Meng, S. Zhou, X. Sui, and X. Hu, “Hybrid Ionogel Electrolytes for Advanced Lithium Secondary Batteries: Developments and Challenges,” *Chemistry, an Asian Journal* 17 (2022): e202200794.

20. J. Le Bideau, L. Viau, and A. Vioux, “Ionogels, Ionic Liquid Based Hybrid Materials,” *Chemical Society Reviews* 40 (2011): 907–925.

21. B. Horstmann, J. Shi, R. Amine, et al., “Strategies Towards Enabling Lithium Metal in Batteries: Interphases and Electrodes,” *Energy & Environmental Science* 14 (2021): 5289–5314.

22. R. Salas, R. Villa, F. Velasco, et al., “Ionic Liquids in Polymer Technology,” *Green Chemistry* 27 (2025): 1620–1651.

23. M. Forsyth, L. Porcarelli, X. Wang, N. Goujon, and D. Mecerreyes, “Innovative Electrolytes Based on Ionic Liquids and Polymers for Next-Generation Solid-State Batteries,” *Accounts of Chemical Research* 52 (2019): 686–694.

24. Y. Zhai, W. Hou, M. Tao, et al., “Enabling High-Voltage “Superconcentrated Ionogel-in-Ceramic” Hybrid Electrolyte with Ultrahigh Ionic Conductivity and Single Li^+-Ion Transference Number,” *Advanced Materials* 34 (2022): e2205560.

25. A. Tsurumaki, R. Rettaroli, L. Mazzapioda, and M. A. Navarra, “Inorganic–Organic Hybrid Electrolytes Based on Al-Doped $Li_7La_3Zr_2O_{12}$ and Ionic Liquids,” *Applied Sciences* 12 (2022): 14.

26. J. W. Suen, N. K. Elumalai, S. Debnath, N. M. Mubarak, C. I. Lim, and M. M. Reddy, “The Role of Interfaces in Ionic Liquid-Based Hybrid Materials (Ionogels) for Sensing and Energy Applications,” *Advanced Materials Interfaces* 9 (2022): 34.

27. L. Chen, Y. Li, S.-P. Li, L.-Z. Fan, C.-W. Nan, and J. B. Goodenough, “PEO/Garnet Composite Electrolytes for Solid-State Lithium Batteries: From “Ceramic-in-Polymer” to “Polymer-in-Ceramic,” *Nano Energy* 46 (2018): 176–184.

28. M. Keller, G. B. Appetecchi, G.-T. Kim, et al., “Electrochemical Performance of A Solvent-Free Hybrid Ceramic-Polymer Electrolyte Based on $Li_7La_3Zr_2O_{12}$ in $P(EO)_{15}LiTFSI$,” *Journal of Power Sources* 353 (2017): 287–297.

29. S. Kim, J. S. Kim, L. Miara, et al., “High-Energy and Durable Lithium Metal Batteries Using Garnet-Type Solid Electrolytes with Tailored Lithium-Metal Compatibility,” *Nature Communications* 13 (2022): 1883.

30. J. A. Isaac, D. Devaux, and R. Bouchet, “Dense Inorganic Electrolyte Particles as A Lever to Promote Composite Electrolyte Conductivity,” *Nature Materials* 21 (2022): 1412–1418.

31. P. Ranque, J. Zagórski, G. Accardo, et al., “Enhancing the Performance of Ceramic-Rich Polymer Composite Electrolytes Using Polymer Grafted LLZO,” *Inorganics* 10 (2022): 81.

32. M. Falco, L. Castro, J. R. Nair, et al., “UV-Cross-Linked Composite Polymer Electrolyte for High-Rate, Ambient Temperature Lithium Batteries,” *ACS Applied Energy Materials* 2 (2019): 1600–1607.

33. Y. Zhang, C. Noè, G. A. Elia, and C. Gerbaldi, “Ionogel Hybrid Polymer Electrolytes Encompassing Room-Temperature Ionic Liquids for 4V-Class Li-Metal Batteries Operating at Ambient Temperature,” *Green Chemistry Letters and Reviews* 17 (2024): 2321247.

34. L. Zhang, Q. Zhuang, R. Zheng, et al., “Recent Advances of $Li_7La_3Zr_2O_{12}$-Based Solid-State Lithium Batteries Towards High Energy Density,” *Energy Storage Materials* 49 (2022): 299–338.

35. P. Jiang, Y. Shi, K. Li, et al., “Recent Progress on The $Li_7La_3Zr_2O_{12}$ (LLZO) Solid Electrolyte,” *Energy Storage Science and Technology* 9 (2020): 523–537.

36. K. Subramanian, G. V. Alexander, K. Karthik, et al., “A Brief Review of Recent Advances in Garnet Structured Solid Electrolyte Based Lithium Metal Batteries,” *Journal of Energy Storage* 33 (2021): 102157.

37. C. Wang, K. Fu, S. P. Kammampata, et al., “Garnet-Type Solid-State Electrolytes: Materials, Interfaces, and Batteries,” *Chemical Reviews* 120 (2020): 4257–4300.

38. Q. Liu, Z. Geng, C. Han, et al., “Challenges and Perspectives of Garnet Solid Electrolytes for All Solid-State Lithium Batteries,*Journal of Power Sources* 389 (2018): 120–134.

39. N. Chen, H. Zhang, L. Li, R. Chen, and S. Guo, “Ionogel Electrolytes for High-Performance Lithium Batteries: A Review,” *Advanced Energy Materials* 8 (2018): 1702675.

40. A. M. Abakumov, S. S. Fedotov, E. V. Antipov, and J. M. Tarascon, “Solid State Chemistry for Developing Better Metal-Ion Batteries,” *Nature Communications* 11 (2020): 4976.

41. M. Dirican, C. Yan, P. Zhu, and X. Zhang, “Composite Solid Electrolytes for All-Solid-State Lithium Batteries,” *Materials Science and Engineering: R: Reports* 136 (2019): 27–46.

42. X. Liu, X. Li, H. Li, and H. B. Wu, “Recent Progress of Hybrid Solid-State Electrolytes for Lithium Batteries,” *Chemistry* 24 (2018): 18293–18306.

43. H. Berg, *Batteries for Electric Vehicles* (Cambridge University Press, 2015), 7–46, Chapter 1, https://doi.org/10.1017/cbo9781316090978.004.

44. B. Roy, U. Pal, M. Kar, and D. R. MacFarlane, “Recent Strategies for Improving The Performance of Ionic Liquids as Battery Electrolytes,” *Current Opinion in Green and Sustainable Chemistry* 37 (2022): 100676.

45. M. Kerner and P. Johansson, “Pyrrolidinium FSI and TFSI-Based Polymerized Ionic Liquids as Electrolytes for High-Temperature Lithium-Ion Batteries,” *Batteries* 4 (2018): 10.

46. M. Kerner, N. Plylahan, J. Scheers, and P. Johansson, “Ionic Liquid Based Lithium Battery Electrolytes: Fundamental Benefits of Utilising Both TFSI and FSI Anions?,” *Physical Chemistry Chemical Physics* 17 (2015): 19569–19581.

47. F. Wu, S. Fang, M. Kuenzel, et al., “Dual-Anion Ionic Liquid Electrolyte Enables Stable Ni-Rich Cathodes in Lithium-Metal Batteries,” *Joule* 5 (2021): 2177–2194.

48. S. Brutti, E. Simonetti, M. De Francesco, et al., “Ionic Liquid Electrolytes for High-Voltage, Lithium-Ion Batteries,” *Journal of Power Sources* 479 (2020): 228791.

49. L. G. Chagas, S. Jeong, I. Hasa, and S. Passerini, “Ionic Liquid-Based Electrolytes for Sodium-Ion Batteries: Tuning Properties To Enhance the Electrochemical Performance of Manganese-Based Layered Oxide Cathode,” *ACS Applied Materials & Interfaces* 11 (2019): 22278–22289.

50. Z. Song, X. Wang, H. Wu, et al., “Bis(Fluorosulfonyl)Imide-Based Electrolyte for Rechargeable Lithium Batteries: A Perspective,” *Journal of Power Sources Advances* 14 (2022): 100088.

51. P. Schmitz, R. Jakelski, M. Pyschik, et al., “Decomposition of Imidazolium-Based Ionic Liquids in Contact with Lithium Metal, *ChemSusChem* 10 (2017): 876–883.

52. K. Li, J. Wang, Y. Song, and Y. Wang, “Machine Learning-Guided Discovery of Ionic Polymer Electrolytes for Lithium Metal Batteries,” *Nature Communications* 14 (2023): 2789.

53. J. Kalhoff, G. G. Eshetu, D. Bresser, and S. Passerini, “Safer Electrolytes for Lithium-Ion Batteries: State of the Art and Perspectives,” *ChemSusChem* 8 (2015): 2154–2175.

54. Y. De Luna, M. Abdullah, S. N. Dimassi, and N. Bensalah, “All-Solid Lithium-Sulfur Batteries: Present Situation and Future Progress,” *Ionics* 27 (2021): 4937–4960.

55. A. Tagliaferro, M. Rovere, E. Padovano, M. Bartoli, and M. Giorcelli, “Introducing the Novel Mixed Gaussian-Lorentzian Lineshape in the Analysis of the Raman Signal of Biochar,” *Nanomaterials* 10 (2020): 1748.

56. M. Kerner, N. Plylahan, J. Scheers, and P. Johansson, “Ionic Liquid Based Lithium Battery Electrolytes: Fundamental Benefits of Utilising Both TFSI and FSI Anions?,” *Physical Chemistry Chemical Physics* 17 (2015): 19569–19581.

57. L. Porcarelli, C. Gerbaldi, F. Bella, and J. R. Nair, “Super Soft All-Ethylene Oxide Polymer Electrolyte for Safe All-Solid Lithium Batteries,” *Scientific Reports* 6 (2016): 19892.

58. *“W. contributors, Settling*,” accessed Norvember 13, 2014, https://en.wikipedia.org/wiki/Settling.

59. C. Liao, X.-G. Sun, and S. Dai, “Crosslinked Gel Polymer Electrolytes Based on Polyethylene Glycol Methacrylate and Ionic Liquid for Lithium Ion Battery Applications,” *Electrochimica Acta* 87 (2013): 889–894.

60. N. N. Sa’adun, R. Subramaniam, and R. Kasi, “Development and Characterization of Poly(1-Vinylpyrrolidone-Co-Vinyl Acetate) Copolymer Based Polymer Electrolytes,” *The Scientific World Journal* 2014 (2014): 254215.

61. S. Duluard, J. Grondin, J. L. Bruneel, et al., “Lithium Solvation and Diffusion in The 1-Butyl-3-Methylimidazolium Bis(Trifluoromethanesulfonyl)Imide Ionic Liquid,” *Journal of Raman Spectroscopy: An International Journal for Original Work in All Aspects of Raman Spectroscopy, Including Higher Order Processes, and Also Brillouin and Rayleigh Scattering* 39 (2008): 627–632.

62. A. S. Pandian, X. C. Chen, J. Chen, et al., “Facile and Scalable Fabrication of Polymer-Ceramic Composite Electrolyte With High Ceramic Loadings,” *Journal of Power Sources* 390 (2018): 153–164.

63. C. Gerbaldi, J. R. Nair, M. A. Kulandainathan, et al., “Innovative High Performing Metal Organic Framework (MOF)-Laden Nanocomposite Polymer Electrolytes for All-Solid-State Lithium Batteries,” *The Journal of Materials Chemistry A* 2 (2014): 9948–9954.

64. D. Brandell, J. Mindemark, and G. Hernández, *Polymer-Based Solid State Batteries*, Chapter 4 (De Gruyter, 2021), 57–77, https://doi.org/10.1515/9781501521140-004.

65. J. Popovic, D. Brandell, S. Ohno, K. B. Hatzell, J. Zheng, and Y.-Y. Hu, “Polymer-Based Hybrid Battery Electrolytes: Theoretical Insights, Recent Advances and Challenges,” *Journal of Materials Chemistry A* 9 (2021): 6050–6069.

66. T. Hou, K. D. Fong, J. Wang, and K. A. Persson, “The Solvation Structure, Transport Properties and Reduction Behavior of Carbonate-Based Electrolytes of Lithium-Ion Batteries,” *Chemical Science* 12 (2021): 14740–14751.

67. J. J. Hu, G. K. Long, S. Liu, G. R. Li, and X. P. Gao, “A LiFSI-LiTFSI Binary-Salt Electrolyte to Achieve High Capacity and Cycle Stability for A Li-S Battery,” *Chemical Communications (Camb)* 50 (2014): 14647–14650.

68. X. Liu, Z. Xiao, H. Peng, et al., “Rational Design of LLZO/Polymer Solid Electrolytes for Solid-State Batteries,” *Chemistry, an Asian Journal* 17 (2022): e202200929.

69. J. Kondo, K. Otani, S. Miyamoto, et al., “Stabilizing the Solid/Liquid Interface in Quasi-Solid Electrolytes via Anion-Derived Interphase Formation in Concentrated Solutions,” *ACS Applied Energy Materials* 8 (2025): 2630–2637.

70. S. Wang, J. Zhang, O. Gharbi, V. Vivier, M. Gao, and M. E. Orazem, “Electrochemical Impedance Spectroscopy,” *Nature Reviews Methods Primers* 1 (2021): 21.

71. M. A. Careem, I. S. M. Noor, and A. K. Arof, *Polymer Electrolytes* (Wiley-VCH, 2020), 23–64, Chapter 2, https://doi.org/10.1002/9783527805457.ch2

72. P. Ghorbanzade, G. Accardo, K. Gomez, et al., “Influence of The LLZO–PEO Interface on the Micro- and Macro-Scale Properties of Composite Polymer Electrolytes for Solid-State Batteries,” *Materials Today Energy* 38 (2023): 101448.

73. K. V. Kravchyk, H. Zhang, F. Okur, and M. V. Kovalenko, “Li-Garnet Solid-State Batteries with LLZO Scaffolds,” *Accounts of Materials Research* 3 (2022): 411–415.

74. L. He, Q. Sun, L. Lu, and S. Adams, “Understanding and Preventing Dendrite Growth in Lithium Metal Batteries,” *ACS Applied Materials & Interfaces* 13 (2021): 34320–34331.

75. A. Mery, S. Rousselot, D. Lepage, and M. Dolle, “A Critical Review for an Accurate Electrochemical Stability Window Measurement of Solid Polymer and Composite Electrolytes,” *Materials (Basel)* 14 (2021): 3840.

76. H. Zhang, F. Chen, O. Lakuntza, et al., “Suppressed Mobility of Negative Charges in Polymer Electrolytes with an Ether-Functionalized Anion,” *Angewandte Chemie International Edition in English* 58 (2019): 12070–12075.

77. K. Liu, X. Li, J. C. Cai, et al., "Design of High-Voltage Stable Hybrid Electrolyte with Ultra-High Li Transference Number," *Chemistry, an Asian Journal* 17 (2022): 30.

78. E. Peled and S. Menkin, "Review—SEI: Past, Present and Future," *Journal of the Electrochemical Society* 164 (2017): A1703–A1719.

79. H.-K. Kim, P. Barai, K. Chavan, and V. Srinivasan, "Transport and Mechanical Behavior in PEO-LLZO Composite Electrolytes," *Journal of Solid State Electrochemistry* 26 (2022): 2059–2075.

80. L. Zou, K. Shi, Z. Xu, Z. Yang, and W. Zhang, "Double-Layer Solid Composite Electrolytes Enabling Improved Room-Temperature Cycling Performance for High-Voltage Lithium Metal Batteries," *ACS Omega* 7 (2022): 994–1002.

81. Y. X. Yao, X. Q. Zhang, B. Q. Li, et al., "A Compact Inorganic Layer for Robust Anode Protection in Lithium-Sulfur Batteries," *InfoMat* 2 (2019): 379–388.

82. C. Xu, B. Sun, T. Gustafsson, K. Edström, D. Brandell, and M. Hahlin, "Interface Layer Formation in Solid Polymer Electrolyte Lithium Batteries: An XPS Study," *Journal of Materials Chemistry A* 2 (2014): 7256–7264.

83. H. Xu, P. H. Chien, J. Shi, et al., "High-Performance All-Solid-State Batteries Enabled by Salt Bonding to Perovskite in Poly(Ethylene Oxide)," *Proceedings of the National Academy of Sciences of the United States of America* 116 (2019): 18815–18821.

Supporting Information

Additional supporting information can be found online in the Supporting Information section. **Supporting Fig. S1:** FESEM images of the HIG series of electrolyte membranes under study: bottom views of (a) HIG-TLiT, (b) HIG-TLiF, (c) HIG-FLiT, and (d) HIG-FLiF. **Supporting Fig. S2:** ATR-FTIR spectra of the electrolyte membranes under study: HIG-TLiT (red), HIG-TLiF (green), HIG-FLiT (magenta), and HIG-FLiF (blue). **Supporting Fig. S3:** The ionic conductivity results, with error bars, of the samples of (a) HIG-TLiT, (b) HIG-TLiF, (c) HIG-FLiT, and (d) HIG-FLiF, in the temperature range from -20 to 80°C (one heating and cooling cycle). **Supporting Fig. S4:** Natural logarithm of the ionic conductivity, ln(σ), as a function of temperature for the hybrid ionogel electrolytes. Symbols represent experimental data, while solid lines correspond to empirical Vogel–Tammann–Fulcher (VTF) fits, included to describe the observed non-Arrhenius temperature dependence of ionic conductivity. **Supporting Fig. S5:** Voltage vs. time profile of HIG-FLiT during Li-plating/stripping test at 25 and 50 μA cm^{-2} for 10 cycles (80 hours) and 5 cycles (20 hours), respectively, in a Li//Li symmetrical cell at ambient temperature. Li electrode area: 0.785 cm^{-2}. **Supporting Fig. S6:** Cyclic voltammetry profiles at scanning rate of 0.1 mV s^{-1} of Li-metal cells assembled with (a) HIG-TLiT, (b) HIG-TLiF, and (c) HIG-FLiF against carbon-coated Al at 25°C, with the inset zoomed-in views. **Supporting Fig. S7:** Charge/discharge cycling behavior of: (a) HIG-FLiT at the current rates of 1C, 2C, and 5C, and (b) HIG-TLiT, (c) HIG-TLiF, (d) HIG-FLiF at the current rates of C/20, C/10, and C/5. The cell tests were undertaken at room temperature (∼21°C). Current density at 1C: 0.13 mA cm^{-2}. **Supporting Fig. S8:** Elemental analysis on cross-section of HIG-FLiT polymerized on LFP cathode (a-d). **Supporting Fig. S9:** XPS spectra of HIG-FLiT surface for C 1s, O 1s, N 1s, F 1s, and Li 1s, before (left-hand-side plots) and after (right-hand-side plots) CV measurement against carbon-coated Al. **Supporting Table S1:** Vogel–Tammann–Fulcher (VTF) fitting parameters (T_0 and R^2) and apparent activation energies ($E_{a,app}$) evaluated locally for the hybrid ionogel electrolytes. **Supporting Table S2:** Output of XPS for HIG-FLiT electrolyte before and after CV tests against cc-Al.